APSB
Acta Pharmaceutica Sinica B

2021
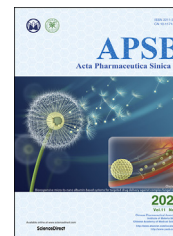
ORIGINAL ARTICLE

Tumor microenvironments self-activated nanoscale metal-organic frameworks for ferroptosis based cancer chemodynamic/photothermal/chemo therapy

Yu Liang[a,b,†], Li Zhang[a,†], Chao Peng[a,b,c,†], Shiyu Zhang[a], Siwen Chen[b], Xin Qian[b], Wanxian Luo[a], Qing Dan[a], Yongyan Ren[d], Yingjia Li[a,*], Bingxia Zhao[b,*]

[a]Department of Medicine Ultrasonics, Nanfang Hospital, Southern Medical University, Guangzhou 510515, China
[b]Guangzhou Key Laboratory of Tumor Immunology Research, Cancer Research Institute, School of Basic Medical Sciences, Southern Medical University, Guangzhou 510515, China
[c]Department of Cerebrovascular Diseases, Zhuhai People's Hospital (Zhuhai Hospital Affiliated with Jinan University), Zhuhai 519099, China
[d]Central Laboratory, Southern Medical University, Guangzhou 510515, China

Abstract   Ferroptosis, as a newly discovered cell death form, has become an attractive target for precision cancer therapy. Several ferroptosis therapy strategies based on nanotechnology have been reported by either increasing intracellular iron levels or by inhibition of glutathione (GSH)-dependent lipid hydroperoxidase glutathione peroxidase 4 (GPX4). However, the strategy by simultaneous iron delivery and GPX4 inhibition has rarely been reported. Herein, novel tumor microenvironments (TME)-activated metal-organic frameworks involving Fe & Cu ions bridged by disulfide bonds with PEGylation (FCSP MOFs) were developed, which would be degraded specifically under the redox TME, simultaneously achieving GSH-depletion induced GPX4 inactivation and releasing Fe ions to produce ROS via Fenton reaction, therefore causing ferroptosis. More ROS could be generated by the acceleration of Fenton reaction due to the released Cu ions and the intrinsic photothermal capability of FCSP MOFs. The overexpressed GSH and H_2O_2 in TME could ensure the specific TME self-activated therapy. Better tumor therapeutic efficiency could be achieved by doxorubicin (DOX) loading since it can not only cause

apoptosis, but also indirectly produce H_2O_2 to amplify Fenton reaction. Remarkable anti-tumor effect of obtained FCSP@DOX MOFs was verified *via* both *in vitro* and *in vivo* assays.

1. Introduction

Ferroptosis, an iron-dependent non-apoptotic form of regulated cell death, which was termed in 2012 by Dixon et al.[1]. Numerous researches have been carried out to uncover the mechanisms of ferroptosis these years. Some regulation mechanisms and signal pathways have already been identified, such as cystine/glutamate antiporter system x_c^- for cystine import[2], the Acyl-CoA synthetase long-chain familymember4 (ACSL4) enzyme about lipid metabolism[3], mevalonate pathway about the production of coenzyme Q10 (CoQ10) for ferroptosis inhibition[4], nicotinamide adenine dinucleotide phosphate (NADPH) and selenium abundance for ferroptosis resistance[5,6]. The defining feature of ferroptosis requires for iron and accumulation of reactive oxygen species (ROS). It is reported that the metabolism of iron impacts ferroptosis sensitivity and the iron is required for the lipid peroxides accumulation to cause the ferroptosis execution[1,7,8]. Moreover, the glutathione (GSH)-dependent lipid hydroperoxidase glutathione peroxidase 4 (GPX4) exerts a pivotal function on ferroptosis through acting as a role of lipid peroxides detoxification with the assistance of the cofactor, GSH[9,10]. Therefore, GSH depletion or GPX4 inhibition could cause elevation of lipid peroxidation for the onset of ferroptosis. Gradually, the non-apoptotic nature makes ferroptosis-based cancer therapy expected to overcome the drawbacks of apoptosis pathways-mediated therapy. Various strategies, such as gene-knockdown technologies[11,12], gene-transfection[13], and small molecular agents (sorafenib[14,15], sulfasalazine[16], artemisinin and its derivatives[17,18]) have been developed to achieve ferroptosis-based therapy by direct or indirect influencing GPX4 activity.

In 2018, Dixon et al.[19] concluded the major strategies to induce cell ferroptosis as by increasing intracellular iron levels or direct/indirect inhibition of the GPX4 activity. Emerging studies based on nanotechnology were reported following these strategies utilizing the unique physicochemical properties of nanomaterials[20]. Several nanoplatforms have been developed by iron delivery, inducing iron-based Fenton reaction[21−23] with overexpressed H_2O_2 in cancer cell[24,25] to generate hydroxyl radical ($\cdot$OH, one kinds of most toxic ROS), such as ferromagnetic nanoparticles (γ-Fe_2O_3 or Fe_3O_4 NPs)[26−28], iron nanometallic glasses[29], iron-containing upconversion nanoparticles[30]. The therapeutic strategy by iron delivery to induce Fenton reaction was also known as chemodynamic therapy[31]. Moreover, some nanoplatforms based on Fe ions containing metal-organic frameworks (MOFs) were also designed utilizing the flexibility and better tumor microenvironments responsiveness of MOFs compared with stable inorganic nanomaterials[32]. For example, a metal−organic network combined with tannic-acid and ferric ions were encapsulated with p53 plasmid (MON-p53), which performed significantly enhance

ferroptosis effect *in vivo* through synergetic ferroptosis/p53 gene therapy[33]. In addition, a reduced iron MOF conjugated with folic acid (rMOF-FA) had achieved folate-mediated tumor targeting and acidic tumor microenvironments induced Fe release for tumor specific ferroptosis[34]. However, researches on MOFs for ferroptosis therapy, especially redox-sensitive MOFs, is still insufficient and their promising future in ferroptosis remains worth exploring further. As it has been reported, the catalytic efficiency of Fe-dependent $\cdot$OH generation could be further improved by auxiliary treatments, such as light[35] and heat[36]. Copper (Cu)-based materials with good photothermal conversion efficiency could result in more $\cdot$OH generation through accelerating Fe-based Fenton reaction by laser-induced heat[37,38]. Interestingly, some recent reports revealed that copper (Cu) ions could also induce the production of $\cdot$OH by Fenton-like reaction[39]. In other words, the fabrication of Fe & Cu dual ions-based MOFs may achieve better ferroptosis efficiency, which has rarely been reported.

Despite of the development of nanoplatforms to induce ferroptosis through iron-based Fenton reaction nanomaterials, some attempts were also carried to induce ferroptosis by suppressing or consuming the overexpressed GSH (up to 10 mmol/L in cancer cell) to inactivate GPX4 indirectly. For instance, an engineered cysteine enzyme was employed to block intratumoral GSH synthesis through reducing L-cysteine, a precursor for the biosynthesis of GSH, thereby obtaining a better therapeutic effect[40]. A tumor-targeted manganese silicate nanobubbles (ASMNs) was successfully synthesized to indirectly induce ferroptosis by high efficient GSH depletion[41]. Some attempts based on MnO_2 nanosystems were also reported to have the ability of consuming intracellular antioxidant GSH for enhancing ROS induced oncotherapy[42,43]. On the other hand, the depletion of GSH would not only induce ferroptosis, but also enhance the ROS-related therapy, such as radio-, chemo-, and photodynamic therapies (PDT), as GSH was well-known as intracellular antioxidant which would consume the cytotoxic ROS to maintain the homeostasis[44−46]. Meng et al.[22] developed a Ce6-loaded glutathione responsive MOF which could cause the intracellular GSH depletion *via* the disulfide−thiol exchange reaction, indirectly causing the GPX4 inactivation-induced ferroptosis, therefore making contributions to the anti-tumor effect of PDT. The therapeutic effect, however, still mainly depended on the PDT effect of Ce6. It would be still worthy to develop novel nanoplatforms for ferroptosis therapy by GSH depletion.

Though successful attempts have been reported by either iron delivery or GPX4 inhibition, only limited work utilized the two strategies simultaneously in one platform for cancer ferroptosis therapy. Liu et al.[47] established core-corona SRF@FeIIITA (SFT) nanoengineering for simultaneous ferrous-supply-regeneration and sorafenib (a GPX4 inhibitor) to induce ferroptosis, thereby

achieving complete tumor elimination with the assistance of imaging-guided PDT. Sang et al.[48] constructed a novel GSH and near infrared (NIR) sensitive micelles to release sorafenib, SPION and NIR photosensitizer Cy7-Hex rapidly at the same time for onset of ferroptosis and lipid hydroperoxides (LPO) burst. These researches, however, still involve photosensitizers to generate ROS and GPX4 inhibitor sorafenib to induce ferroptosis.

Herein, for the first time, redox tumor microenvironment (TME)-activated metal−organic framework were constructed with Fe & Cu dual ions bridged by disulfide bonds with PEGylation (FCSP MOFs). These FCSP MOFs can be accumulated in the tumor site by the typical enhanced permeability and retention (EPR) effect, where GSH depletion and the release of Fe & Cu ions occurred due to the breakage of disulfide linkers under the GSH overexpressed TME. With the assistance of GSH depletion, more toxic ROS generated by the self-activated Fenton or Fenton-like reaction between the large amount of the released Fe & Cu ions and the endogenous H_2O_2 could take effect to achieve ferroptosis based chemodynamic therapy. Moreover, the depletion of GSH resulted in the highly efficient GPX4 inactivation in tumor cells. What's more, the appeared adorable photothermal effect of FCSP could be used not only for mild photothermal therapy, but also to further accelerate the Fenton reaction and enhance the therapeutic effect. To achieve better tumor therapeutic efficiency, doxorubicin (DOX), a common chemotherapeutics, was loaded into the structure, which could not only induce chemotherapy, but also generate H_2O_2 to further amplify the ferroptosis based chemodynamic therapy efficacy[49]. Taking the synergy of GSH-depletion assistant GPX4 inactivation and iron-dependent Fenton reaction induced ferroptosis, mild hyperthermia, and chemotherapy, excellent anti-tumor efficiency was achieved both in vitro and in vivo with minimized damage to normal tissues.

2. Materials and methods

2.1. Materials and reagents

Iron (II) chloride tetrahydrate ($FeCl_2 \cdot 4H_2O$), dimethyl sulfoxide (DMSO), pyridine and triethanolamine (TEA) were purchased from Macklin, Shanghai, China. Cupric chloride dihydrate ($CuCl_2 \cdot 2H_2O$) was purchased from Aladdin, Shanghai, China. Dithiodiglycolic acid was produced by Xiya reagent, Shandong, China. N,N-dimethylformamide (DMF) was obtained from Chemical Reagent Factory, Guangzhou, China. Poly-vinylpyrrolidone (PVP, MW = 40,000) was from solarbio company in Beijing, China. Poly (ethylene glycol) methyl ether (mPEG-NH$_2$, MW = 2000) was synthesized by Yare Biotech, Shanghai, China. Poly-(maleic anhydride-alt-1-octadecene) (PMHC18) was from Sigma−Aldrich, USA. Doxorubicin hydrochloride (DOX) was obtained from Sangon Biotech Co., Ltd., Shanghai, China. The cell lines of 4T1 and MC3T3-E1 were donated by the Research Center of Clinical Medicine in Nanfang Hospital (Guangzhou, China). LIVE/DEAD Cell Imaging Kit was from KeyGEN Biotech, Nanjing, China. Dichlorofluorescein diacetate (DCFH-DA) was obtained from the company of Meilun Biotech, Dalian, China. Anti-GPX4 antibody (ab125066) was from Abcam and secondary antibody IgG/HRP (bs-0295G-HRP) was from Beijing Biosynthesis biotechnology Co., Ltd. BODIPY 581/591 C11 was from Invitrogen, USA. Annexin V-FITC apoptosis detection kit was purchased from Beyotime, Shanghai, China. Dulbecco's modified Eagle's medium (DMEM) was purchased from Gibco, Thermo Fisher, America. Other materials and reagents were purchased from Sigma−Aldrich, USA.

2.2. Preparation of Fe·Cu-SS (FCS) MOFs

A mixture of $FeCl_2 \cdot 4H_2O$ solution, $CuCl_2 \cdot 2H_2O$ solution (the total amount of Fe^{2+} and Cu^{2+} was 42.5 μmol in DMF), PVP (300 mg), dithiodiglycolic acid (52 μL, 100 mg/mL in DMF), and different amount of triethylamine (TEA) was dispersed in a graduated cylinder. DMF/ethanol solution was then added until the volume reached up to 13 mL ($V_{DMF}/V_{ethanol} = 5/3$). The solution was then transferred to a 50 mL Teflon-lined stainless autoclave after dispersed ultrasonically and reacted at 150 °C for 12 h. The final obtained FCS products were resuspended in ddH$_2$O after being washed and centrifuged with ethanol or water until the supernatant was clear.

2.3. Drug loading and surface modification of FCS MOFs

Firstly, Fe·Cu-SS@DOX (FCS@DOX) were prepared by adding DOX (5 mg/mL, 200 μL) into the 10 mL FCS dispersion (0.5 mg/mL in ddH$_2$O), then the obtained solution was stirred overnight under light-sealed conditions. The C18PMH-mPEG was prepared as the previous method[50]. 5 mL C18PMH-mPEG polymer (3 mg/mL in chloroform) was sonicated for 30 min in a round-bottom flask. Then, thin film of C18PMH-mPEG was acquired by vacuum rotary evaporation. Subsequently, FCS@DOX dispersion was dumped into the round-bottom flask. After ultrasonic processing for 30 min, the FCSP@DOX with surface modification were purified through removing the residual reactants by centrifugation. In order to calculate the loading capacity (Q) of DOX, the residual DOX content (R_{DOX}, μg) of the collected supernatant was calculated by UV−Vis absorption at 480 nm. The DOX loading capacity (Q) was then calculated as $Q (\%) = (1000-R_{DOX})/(6000-R_{DOX}) \times 100$.

2.4. Characterization

A JEOL JEM-2100 F TEM was applied for transmission electron microscopy (TEM) and High-angle annular dark-field scanning TEM (HAADF-STEM)-based elemental mapping at an acceleration voltage of 200 kV. The size distribution of the MOFs was carried out by using a Malvern Zetasizer Nano ZS instrument (Malvern Instruments, Malvern, UK). An UV-2600 UV−Vis spectrophotometer from Shimadzu was applied to note the UV−Vis absorption spectra. An absorption analyzer Quantach-rome instruments (Florida, USA) was used to performed N$_2$ adsorption/desorption isotherms (BET). X-ray diffraction (XRD) was detected by a Thermo Fisher ARL EQUINOX 3000 X-ray diffractometer. Fourier transform infrared spectroscopy (FTIR) was applied by a Thermo Fisher Nicolet 6700.

2.5. Photothermal performance of FCS MOFs

To determine the photothermal effect, 200 μL FCS MOFs with different concentrations were exposed to an 808 nm laser (Shanghai Xilong Optoelectronics Technology Co., Ltd., China) for 5 min at different laser powers density. An infrared thermal imaging system (FLIR E50, USA) was used to note the temperature changes of the solutions. Finally, photothermal stability of FCS MOFs was determined by irradiating FCS MOFs PBS solution for five lasers on−off cycles. Ultimately, the influence of 10 mmol/L GSH to the photothermal property of FCSP MOFs was

explored by irradiating 200 μL 62.5 μg/mL FCSP at different laser power density before and after incubation with 10 mmol/L GSH.

2.6.   In vitro TME-activated experiment

For exploring GSH-triggered cleavage of the FCSP MOFs structure, FCSP MOFs solutions were incubated in PBS with or without 10 mmol/L GSH. At predetermined time intervals, the structures were observed by TEM (JEOL). For exploring the GSH depletion capability of FCSP MOFs, FCSP MOFs solutions were incubated with 10 mmol/L GSH. At predetermined time intervals, 10 μL supernatant was taken out for analysis of GSH and oxidized glutathione (GSSG) amount by Liquid chromatography-mass spectrometry (ThermoFisher Scientific, Prelude SPLC + TSQ LC–MS/MS, USA).

The Rhodamine B (RhB) were applied to test the ·OH generation ability of FCSP MOFs because RhB could be transformed into colorless substance after being degraded by ·OH. The change at 553 nm absorbance was recorded to measure the RhB degradation. The potential influence from FCSP MOFs on the absorbance was avoided by centrifugation before measurement and the absorbance was normalized to the control.

Considering DOX would be released along with the breakage of MOFs structure, drug release kinetics of FCSP@DOX with varying condition were then researched. 1 mL FCSP@DOX (DOX concentration: 0.5 mg/mL) in a dialysis bag (MWCO 14800) was on dialysis in 100 mL PBS under light-sealed conditions at room temperature with or without 10 mmol/L GSH at pH = 7.4 or 5.8. At predetermined time intervals, the medium (1 mL) was taken out for analysis by UV–Vis spectrometer at 480 nm (Shimadzu), meanwhile the same volume of fresh PBS solutions were supplemented.

2.7.   In vitro cellular experiment

Cytotoxicity of the materials was evaluated using the methyl thiazolyl tetrazolium (MTT) assay in 4T1 and MC3T3-E1 cells. Typically, under a humidified atmosphere with $1\% \ O_2$, $5\% \ CO_2$, $94\% \ N_2$ at 37 °C, 4T1 and MC3T3-E1 cells were seeded in a 96-well culture plates at a density of 1×10^4 cells per well. After the cells were attached to the plates, various concentrations of FCSP MOFs in 100 μL culture media were used to replace the previous medium. With another 24 h incubation, the mixture of 10 μL MTT (5 mg/mL in PBS) and 100 μL culture media were added to replace the previous culture media, and then the cells were incubated for another 4 h. After replacing the media with 150 μL DMSO per well, a BioTek microplate reader (BioTek, USA) was applied to monitor the absorbance of formazan at 495 nm.

GPX4 protein expression level was analyzed by Western blot. In brief, 4T1 cells were seeded on a 6-well plate at 37 °C overnight in an atmosphere of $1\% \ O_2/5\% \ CO_2/94\% \ N_2$. Different concentrations of FCSP MOFs were added and cultured for 24 h. The collected cell lysates were evaluated by polyacrylamide gel electrophoresis.

Subsequently, lipid peroxidation levels were assessed by BODIPY 581/591 C11 dye. Cells were seeded in 6-well plates in triplicate 24 h prior to treatment, pretreated with different concentrations of FCSP MOFs for 24 h, and then 1 μmol/L BODIPY 581/591 C11 in fresh culture medium was added to each well. After incubation for 30 min, the cells were observed by a fluorescent microscope (Nikon Eclopse T1-U, Tokyo, Japan). Lipid peroxidation levels were further analyzed by flow cytometry using

a flow cytometry (BD LSRFortessaTM Cell Analyzer, USA). In order to further explore the mechanism of FCSP MOFs, the cell apoptosis was assessed by flow cytometry using an Annexin V-FITC apoptosis detection kit.

To further explore the intracellular ROS generation, a ROS probe, DCFH-DA was applied. For fluorescent microscope, 4T1 cells (3×10^5 per well) in 2 mL of medium were seeded into a 6-well culture plates at 37 °C in an atmosphere of $1\% \ O_2$, $5\% \ CO_2$, $94\% \ N_2$. After being attached to the plates, cells were incubated with 2 mL fresh medium of DMEM, FCSP, FCSP+10 mmol/L GSH, FCSP@DOX, FCSP@DOX+10 mmol/L GSH, then with or without 808 nm laser irradiation (5 min, 0.7 W/cm^2) respectively after another 4 h incubation, followed by staining of DCFH-DA assay kit for 2 h. Lastly, a fluorescent microscope was used to observe the cells. For the analysis of flow cytometry, 4T1 cells were harvested and washed with PBS for flow cytometry after being disposed as mentioned above. As for ROS generation ability of single FCSP, DCFH-DA assay kit was used to detect the amount of ROS generated by different concentration of FCSP in 4T1 cells.

Both fluorescent microscope and flow cytometer were applied to examine the cellular uptake experiments of FCSP@DOX. Firstly, to confirm the intracellular GSH-induced DOX release of FCSP@DOX in high level GSH cancer cells, two cell lines, including a cancer cell (4T1) with higher GSH concentration and a normal cell line (MC3T3-E1) with lower GSH were chosen. Detailly, 4T1 cells and MC3T3-E1 cells were seeded in 6-well plates (2×10^5 cells per well). After being cultured for 24 h, 2 mL fresh medium containing FCSP@DOX was used to replace the medium. After 12 h, the fluorescence intensity of cells was detected by fluorescent microscope and flow cytometry analysis. Next, the influence of NIR against the cellular uptake was further explored, 4T1 cells were seeded in 6-well plates (2×10^5 cells per well). After being cultured for 24 h, 2 mL fresh medium containing FCSP@DOX and FCSP@DOX + NIR was used to replace the medium. After 4 h, 808 nm laser was applied to the cells of the irradiation groups (NIR, 0.7 W/cm^2) for 5 min. After incubation for another 2 h, the fluorescence intensity of cells was evaluated by fluorescent microscope and a flow cytometer. To measure the cancer cells treatment efficiency in vitro, 4T1 cells were seeded into 96-well culture plates at a density of 1×10^4 cells per well. Then, the following treatments were exposed to the cells: control, NIR, FCSP, FCSP + NIR, FCSP +10 mmol/L GSH, FCSP +10 mmol/L GSH + NIR, FCSP@DOX, FCSP@DOX + NIR, FCSP@DOX +10 mmol/L GSH, FCSP@DOX +10 mmol/L GSH + NIR. After incubation for 4 h, 808 nm laser was applied to the cells for 5 min (0.7 W/cm^2) in the laser irradiation groups (NIR). After incubation for another 24 h, the viability of cells was then measured via the MTT assay.

2.8.   In vivo cancer treatment

Thirty-six female 4–6 weeks old BALB/c mice were purchased from Southern Medical University Laboratory Animal Center (Guangzhou, China). All animal experiments procedures were performed in accordance with the regulations of Animal Ethics Committee based on Southern Medical University Animal Studies Committee. 5×10^6 4T1 cells in PBS were subcutaneously injected on the right rear leg to initiate the tumors. These mice were randomly divided into six groups ($n = 6$, each group) when the volume of tumors reached 50 mm^3: control, FCSP, FCSP + NIR, FCSP@DOX, FCSP@DOX + NIR, and free DOX.

24 h post-injection of different medicaments, the NIR treatment groups were irradiated by 808 nm for 10 min (0.7 W/cm^2) with the observation of an IR thermal camera. A digital caliper was used to monitor the length and width of the tumors. Then the anti-tumor effectiveness was assessed by calculating the tumor volumes $(V) = $ Length $\times$ Width^2/2. $V/V_0 \times 100\%$ was defined as relative tumor volume, where V_0 was the initial tumor volume pre-treatment. Body weights were also monitored every 2 days post-treatment. After treatment, tumor tissues of each group were stained with hematoxylin and eosin (H&E) and TUNEL to observe tumor morphology and apoptosis. In order to affirm the biosafety of FCSP MOFs, the main tissue pathological staining from PBS and FCSP@DOX + NIR group were obtained on the third day after the treatment. As for validating the mechanism of FCSP MOFs, the GPX4 level of tumor in every group was measured by Western blot.

### 2.9. In vitro and in vivo magnetic resonance (MR) and photoacoustic (PA) imaging

For in vitro MR/PA imaging, MOFs were dissolved with 1% agar solution to create different concentrations FCSP. Samples were transferred into 1.5 mL Eppendorf tubes and allowed to set when the mixture was fully dissolved. A Bruker Biospin MRI GmbH scanner (PharmaScan70/16 US, WI, USA) with scanning sequence for fast field echo FFE (TR = 2500, TE = 35, slice thickness = 1.0 mm), were used to obtained MR image. The photoacoustic imaging system (VEVO 2100, FUJIFILM Visual Sonics, USA) were employed to gain photoacoustic imaging of various MOFs concentrations. In vivo MR/PA images of 4T1 tumor-bearing mice were obtained before and after intratumoral injection of FCSP solutions.

3. Results and discussion

3.1. Synthesis and characterization of FCSP@DOX MOFs

The TME self-activated biodegradable MOFs (FCSP@DOX) for synergetic ferroptosis based chemodynamic/photothermal/chemo therapy is schematically described in Scheme 1. Hydrothermal method was employed to synthesize FCS MOFs with Fe & Cu dual ions bridged by disulfide bonds. According to the transmission electron microscopy (TEM) images, FCS MOFs showed flower-like structures and a homogeneous size distribution of 127.53 $\pm$ 24.47 nm (Fig. 1A). High-angle annular dark-field scanning TEM (HAADF-STEM)-based elemental mapping revealed that the as-prepared FCS MOFs contained Fe, Cu and S elements (Fig. 1A). X-ray diffraction patterns (XRD) were used to demonstrate the structure of the as-prepared FCS MOFs. The

results showed that the diffraction pattern matched with CuFe$_2$S$_3$ without any other representative phases detected (Supporting Information Fig. S1). The formation of the FCS MOFs structures could be influenced by the Fe/Cu ratio and TEA concentration. As shown in Supporting Information Fig. S2, the average size of FCS MOFs varied along with different proportion of Fe and Cu, and had a general trend of increasing with the increase of Fe. The flower-like MOFs structures could be obtained when the Fe/Cu value was larger than 1. With the constant Fe/Cu ratio, the average size of FCS MOFs would decrease from 200 nm to 50 nm along with increasing TEA amount (Supporting Information Fig. S3). Thus, the average size of these MOFs can be simply tuned by varying the ratio of Fe/Cu or the TEA amount. Subsequently, MOFs with average diameter about 100 nm were chosen for subsequent experiments because of its good morphology and structure. N$_2$ adsorption/desorption isotherm curves (BET) analysis indicated that FCS MOFs had a pore volume of 0.287 cm^3/g, a surface area of 71.05 m^2/g, and adsorption average pore width of 8.36 nm, respectively (Fig. 1B), suggesting their great potential to be applied for drug loading and delivery. DOX, a typical chemotherapy drug, was therefore loaded into the pores of FCS MOFs through hydrophobic interaction (FCS@DOX). Afterwards, C18PMH-mPEG was therefore be applied to modify the surface of the FCS MOFs and FCS@DOX MOFs (named as FCSP and FCSP@DOX), as it has been reported that properly modification with amphiphilic surfactant might endow the as-prepared MOFs with good water solubility and biocompatibility, avoiding rapid removal by the body's immune system, leading to high tumor intake through the enhanced permeability and retention (EPR). To verify the successful surface modification of PEG on FCS MOFs, the Fourier transform infrared (FTIR) spectra of the FCS, C18PMH-mPEG and FCSP were obtained. As showed in Supporting Information Fig. S4, the FCSP MOFs owned both the characteristic peaks of FCS MOFs and C18PMH-MPEG, which illustrated the successful modification of C18PMH-mPEG. After being modified with C18PMH-mPEG, FCSP showed greater dispersibility and suspensibility than FCS after PEGylation as could be seen from the appearance changes after storage in PBS along with time (Supporting Information Fig. S5). The UV−Vis spectra demonstrated that FCSP@DOX exhibited an absorption peak at 480 nm (Fig. 1C), the same as the characteristic absorption peaks of DOX, confirming the successful loading of DOX into the MOFs. The drug loading capacity of DOX were calculated as 8.92%. In addition, the FCSP@DOX MOFs also displayed strong absorbance in the NIR window (Fig. 1C), denoting that they may have promising photothermal performance. To evaluate the photothermal ability of the as-prepared MOFs, the temperature changes versus different concentrations FCSP@DOX aqueous dispersions were recorded under 808 nm laser irradiation within 5 min. Remarkable photothermal stability of the FCSP MOFs was demonstrated within at least five laser on−off cycles
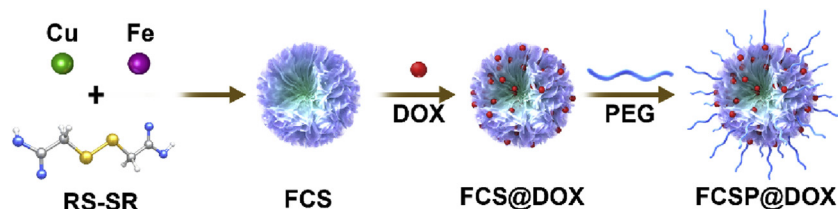
Scheme 1 Schematic illustration of the synthesis of TME self-activated FCSP@DOX MOFs for ferroptosis based cancer chemodynamic/photothermal/chemo therapy.
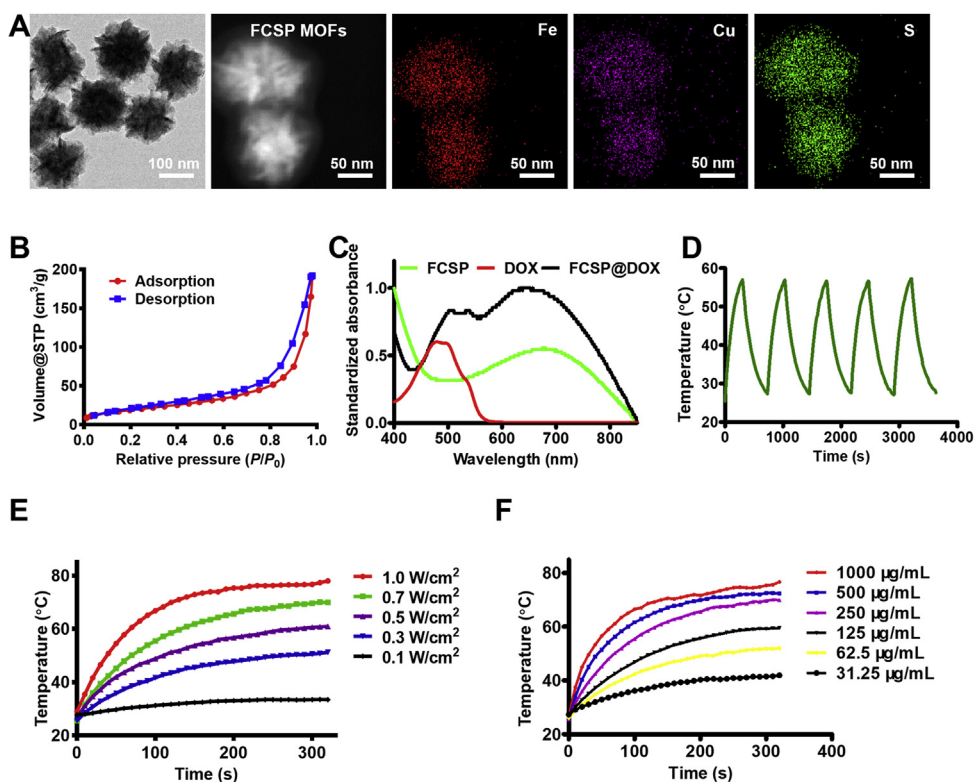
Figure 1 (A) TEM images of FCS MOFs and STEM−EDS elemental maps of FCSP MOFs. (B) Nitrogen adsorption−desorption isotherms of FCS MOFs. (C) UV−Vis spectra of FCSP MOFs, FCSP@DOX MOFs and free DOX. (D) Photothermal stability of FCSP MOFs within five cycles of NIR laser irradiation. (E) Temperature change curses of the FCSP MOFs aqueous dispersion at different power density at the same concentrations of 250 μg/mL. (F) Temperature change curses of the FCSP MOFs aqueous dispersion at different concentrations at the power density of 0.7 W/cm^2.

(Fig. 1D). The temperature of the FCSP@DOX MOFs aqueous dispersions presented concentration and power density dependent temperature increases under 808 nm laser irradiation as shown in Fig. 1E and F, and Supporting Information Fig. S6.

3.2. In vitro TME-activated GSH depletion and fenton reaction

Considering the existence of GSH-sensitive disulfide bonds in the MOFs, it could be presumed that a redox TME-triggered GSH depletion and cleavage of the MOFs structure might happen. To verify this, the as-prepared MOFs were incubated in PBS with or without 10 mmol/L GSH to proof the redox TME responsiveness. As expected, a time-dependent MOFs decomposition could also be observed in PBS with 10 mmol/L GSH while no obvious morphology change could be observed without GSH as shown in the TEM pictures (Fig. 2A and Supporting Information Fig. S7). At the same time, it could be discovered by the liquid chromatography-mass spectrometry (LC−MS) results that GSH depletion was activated spontaneously as GSH was gradually transformed into oxidized glutathione (GSSG) along with times (Fig. 2B). These results indicated that the as-prepared MOFs could activate the depletion of GSH together with the decomposition of the mesoporous structure, leading to the release of dual ions and drugs.

As the TME-activated MOFs degradation happened, Fe and Cu dual ions would be simultaneously released for the production of toxic ·OH via Fenton or Fenton-like reaction. The ability of the Fe & Cu dual ions to generate ·OH was then investigated by the rhodamine B (RhB) decolorization experiment because the red color RhB could be degraded into colorless by ·OH. Apparent

RhB degradation in Fe^{2+}/Cu^{2+} group could be observed (∼4.9%) suggesting that Fe & Cu ions could indeed react with H$_2$O$_2$ to generate ·OH via Fenton and Fenton-like reaction (Fig. 2C and D). After the addition of GSH, the ·OH generation was largely suppressed (∼85.1%), indicating that generated ·OH was captured by the antioxidant GSH. FCSP MOFs, on the other hand, could only generate a little amount of ·OH due to the reaction of the surface ions without the existence of GSH (∼75.2%). Activated by the GSH-rich environment, FCSP MOFs showed much more ·OH generation (∼43.8%) since the GSH-induced release of Fe & Cu ions exposure to H$_2$O$_2$ and the depletion of GSH. These results demonstrated that the MOFs could exhibit specific redox-TME activated generation of toxic ·OH for ferroptosis-based cancer chemodynamic therapy. Moreover, to investigate whether external stimuli could accelerate the Fenton reaction for more ·OH generation, the temperature of the solutions was firstly increased to 46 °C. The absorbance of RhB exhibited further decrease for either H$_2$O$_2$+FCSP (∼75.2%) or H$_2$O$_2$+FCSP + GSH (∼43.8%) (Fig. 2E and F), illustrating that hyperthermia can efficiently promote Fenton reaction for more ·OH generation. Then, the addition of Cu^{2+} into H$_2$O$_2$+FCSP or H$_2$O$_2$+FCSP + GSH groups further facilitated the decolourization of RhB to 59.0% and 29.1%, respectively (Fig. 2E and F), which demonstrated that the addition of Cu^{2+} could lead to more ·OH generation, and the fabrication of Fe & Cu dual ions into FCS MOFs was conducive to achieve better ferroptosis effect. Noticeably, it could also be seen that only very slight changes could be observed in photothermal performance of the MOFs after being incubated with 10 mmol/L GSH (Supporting Information
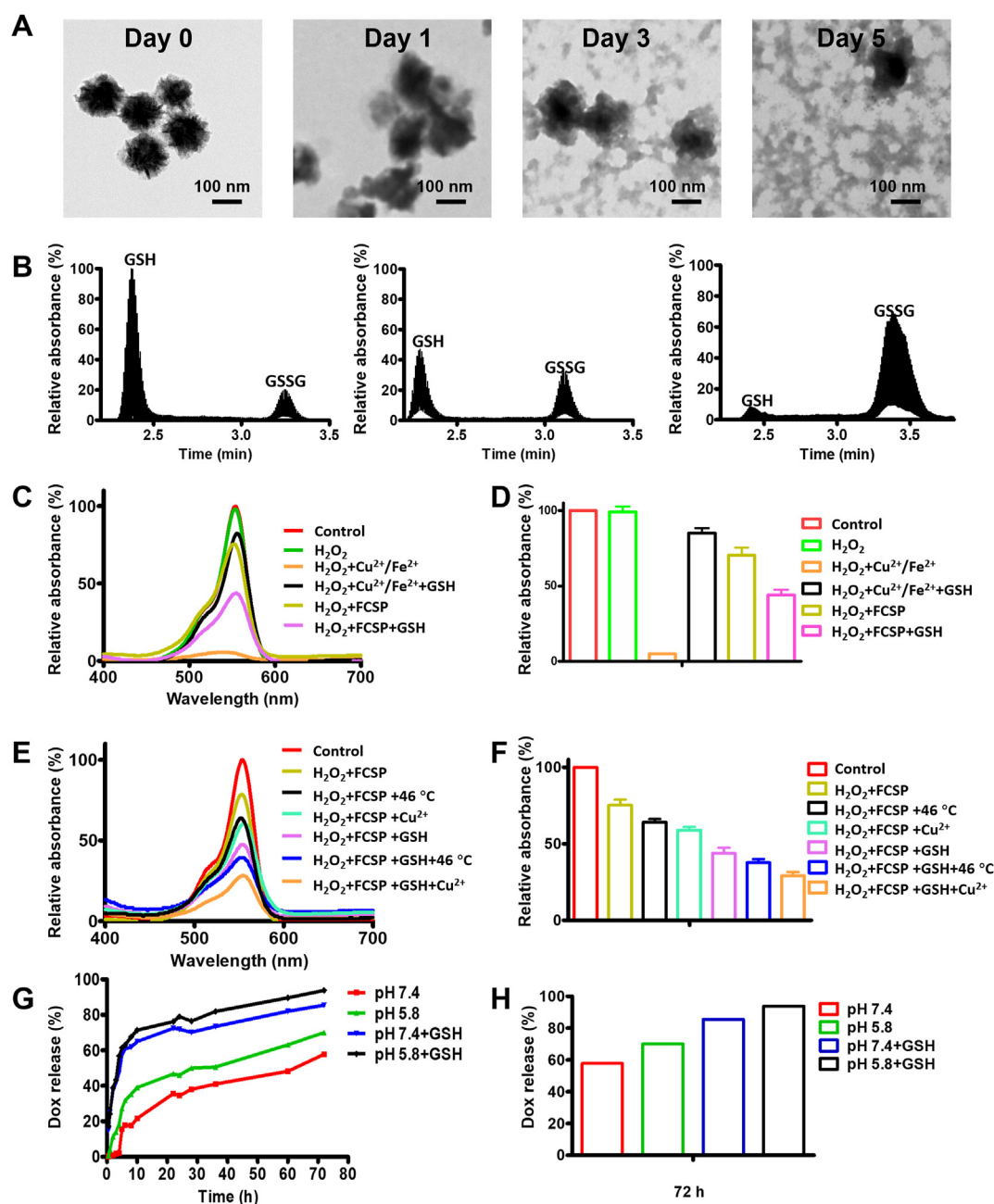
Figure 2 (A) TEM images of biodegradable FCSP MOFs immersed in 10 mmol/L GSH aqueous solution for Days 0, 1, 3 and 5. (B) Liquid chromatography-mass spectrometry (LC−MS) results about the reaction between FCSP MOFs and GSH after 0, 3, and 5 days. (C) UV−Vis analysis of the Fenton reaction for RhB decolorization of different groups to demonstrate the ability of ·OH generation and (D) their relative quantification at 553 nm. (E) UV−Vis analysis of the Fenton reaction for RhB decolorization of different groups to demonstrate the ability of heat and Cu^{2+} enhanced ·OH generation and (F) their relative quantification at 553 nm. (G) Release kinetics of DOX from FCSP@DOX MOFs in PBS at different pH without or with 10 mmol/L GSH and (H) their relative quantification of DOX release at 72 h. Date are presented as mean ± SD ($n = 3$).

Fig. S8), demonstrating that the photothermal property of FCSP MOFs would not be influenced by the GSH-induced degradation of the MOFs. These results suggest that the NIR-induced hyperthermia could always be achieved as long as the MOFs were accumulated in the tumor site, whether the degradation of MOFs happened or not. Therefore, the NIR-induced hyperthermia could also be applied to accelerate Fenton reaction for more ·OH generation, enhancing the ferroptosis based cancer chemodynamic therapy.

Simultaneously with the GSH-triggered breakage of the MOFs and enhanced ferroptosis based chemodynamic therapy, the loaded DOX might also be gradually released, fulfilling the redox-activated drug release. *In vitro* drug release of FCSP@DOX under various conditions was then carried out. The release efficiency of FCSP@DOX MOFs was evaluated under PBS with or without 10 mmol/L GSH (pH 7.4 and pH 5.8). As expected, drug release was dramatically increased in the presence of GSH, due to the disassembly of the MOFs structures (Fig. 2G and H). The release
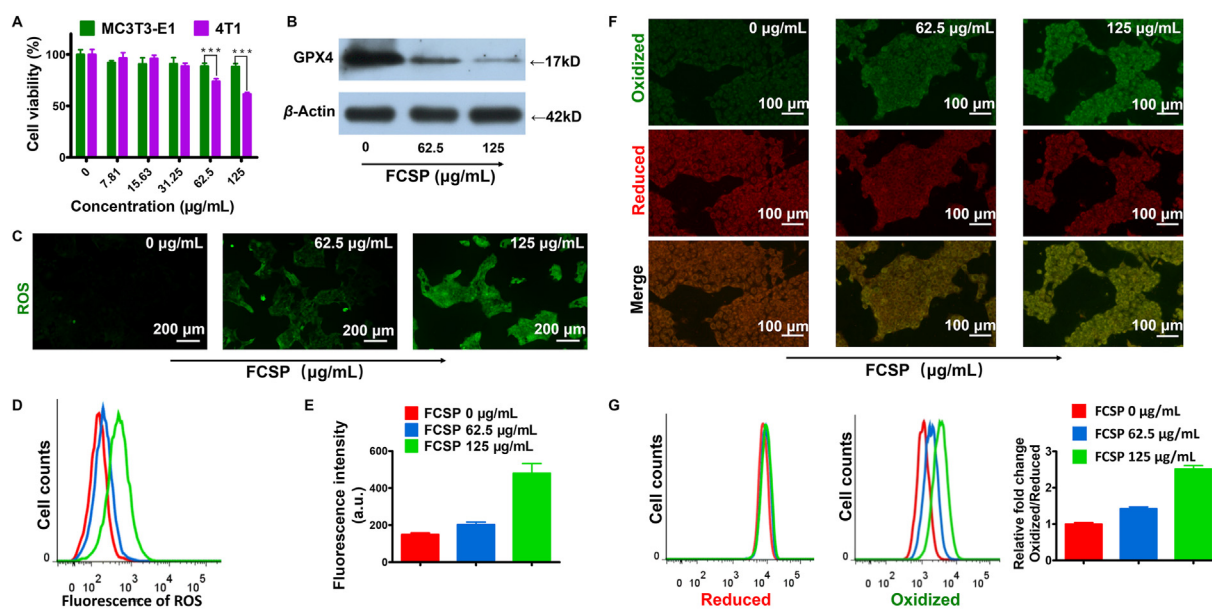
Figure 3 (A) Cell viabilities of MC3T3-E1 or 4T1 cells after incubation with FCSP MOFs at different concentration, date are presented as mean $\pm$ SD ($n = 6$). ***$P < 0.001$. (B) Western blot results of GPX4 expression level in 4T1 cells after treatment with different concentration FCSP MOFs. (C) DCFH-DA assay of 4T1 cells treated with different concentration FCSP (0, 62.5, and 125 μg/mL), scale bar = 200 μm, and (D) their corresponding flow cytometry analyses and (E) relative fluorescence intensity (a.u.). Date are presented as mean $\pm$ SD ($n = 3$). (F) Fluorescence images of 4T1 cells treated with different MOFs formulations, C11-BODIPY was used to assess lipid peroxidation. Scale bars = 100 μm (G) Their corresponding flow cytometry analyses. The panel from left to right represented the fluorescence intensity of reduced lipid, oxidized lipid, and relative fold changes of lipid peroxidation in Oxidized/Reduced, respectively. Date are presented as mean $\pm$ SD ($n = 3$).

amount of DOX under the condition of 10 mmol/L GSH solution reached more than 85% whether at pH 5.8 or pH 7.4 after 72 h, which was much higher than that without GSH (70% or 57%). In addition, the release of DOX at acid condition (pH 5.8) was also slightly higher than that at neutral condition (pH 7.4), suggesting a pH-responsive drug release ability, which might be resulted from the decrease of the electrostatic interaction between FCSP@DOX and DOX under the acid environments, similar to that in other nano-delivery platforms. Taking into account of the redox and acid tumor microenvironments, the GSH/pH dual-responsive DOX release property of FCSP@DOX MOFs was preferred for achieving specific tumor site release, therefore enhancing the therapeutic efficiency.

3.3. In vitro cellular experiments of redox TME self-activated ferroptosis based chemodynamic/photothermal/chemo therapy

As it is well-known, biocompatibility is the basic factor prior to bio-application. In our experiment, MTT assay was firstly implemented to assess the cytotoxicity of the as-prepared FCSP MOFs in murine normal cells MC3T3-E1 and murine breast cancer cells 4T1. No significant inhibition of the cell viability could be found at the experimental concentration for MC3T3-E1 cells, while much greater cytotoxicity against 4T1 cancer cells was observed (Fig. 3A), indicating that the FCSP MOFs possessed well biocompatibility to normal cells and showed specific toxicity to the cancer cells. Cell apoptosis was then assessed and the results showed that the proportion of apoptosis was less than 20% even in the highest concentration FCSP MOFs group, which demonstrated that apoptosis was not the main reason causing cell death (Supporting Information Fig. S9). As it is known to all, GSH level in solid tumor cells is higher than that in normal cells. Since the

ability of FCSP in consuming GSH had been verified above, the cytotoxicity to 4T1 cells might be caused by the GPX4 inactivation-induced ferroptosis, as GSH depletion could inactivate GPX4 and prevent the reduction of lipid hydroperoxides. The GPX4 expression level of 4T1 cells was then determined by Western blot. As expected, the GPX4 protein expression level decreased along with the increased concentration of FCSP (Fig. 3B), showing that FCSP can down-regulate GPX4 expression through depleting its cofactor GSH. As it was designed, the as-prepared MOFs could induce ferroptosis therapy by simultaneously GPX4 inhibition and iron delivery for ROS generation via Fenton reaction. The generation of ROS was then assessed by using an ROS probe DCFH-DA. As shown in Fig. 3C, the green fluorescence from DCF become brighter and brighter along with increasing FCSP concentrations, demonstrating the generation of ROS under the tumor microenvironment. The level of ROS was further quantified by flow cytometry analysis and was consistent with the fluorescence images (Fig. 3D and E). As it has been concluded, the accumulation of lipid peroxidation is the hallmark of ferroptosis[19]. Herein, lipid peroxidation induced by FCSP MOFs in 4T1 cells was assessed (Fig. 3F and G). As it could be noted, the green fluorescence of oxidized lipid became more and more evident along with increasing FCSP concentrations while the red fluorescence of reduced lipid had no significant change, demonstrating that the level of lipid peroxidation had increased with increasing FCSP concentrations. The results of flow cytometry analysis further verified that FCSP could increase lipid peroxidation. In general, the FCSP MOFs possess the potential to be used as ferroptosis inducer.

As it has been reported, the intracellular high level GSH in cancer cells would promote the intracellular release of drug after endocytosis in GSH-responsive drug-loaded nanoparticles[51–53].
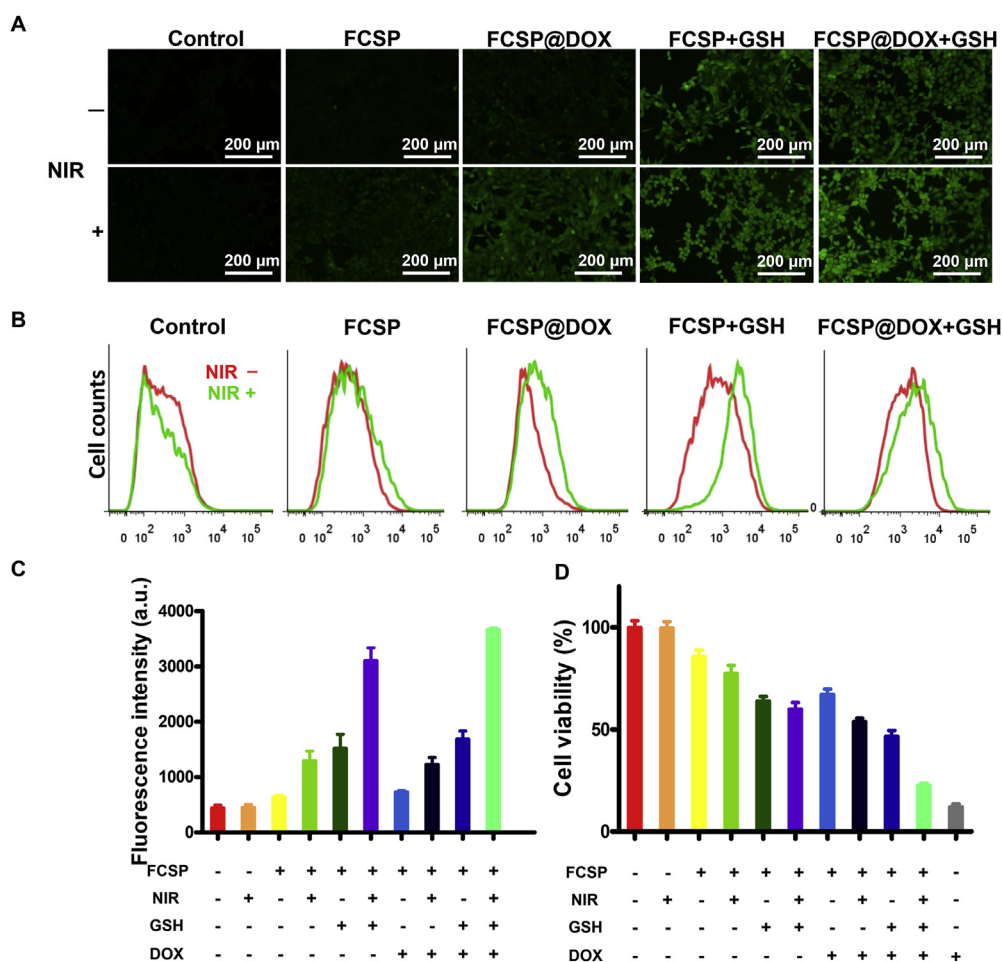
Figure 4 (A) Fluorescence images of 4T1 cells treated with different MOFs formulations with or without NIR, DCFH-DA was used to detect ROS generation. Scale bars = 200 μm and (B) their corresponding flow cytometry analyses and (C) relative fluorescence intensity (a.u.). (D) Cell viabilities of 4T1 cells after treatment with different MOFs formulations with or without NIR. Date are presented as mean ± SD ($n = 3$).

Considering the GSH-responsive DOX release property of FCSP@DOX MOFs has been well confirmed above (Fig. 2G and H), two cell lines, including a cancer cell (4T1) with higher GSH concentration and a normal cell line (MC3T3-E1) with lower GSH were chosen to confirm the intracellular GSH-induced DOX release of FCSP@DOX in high level GSH cancer cells. The results in the Supporting Information Fig. S10 show that the fluorescence intensity of 4T1 was significantly stronger than that of MC3T3-E1 cells, indicating that the DOX could not output enhanced signals with lower GSH in the normal MC3T3-E1 cells. Therefore, these stimuli-responsive FCSP@DOX MOFs might have promising potential for highly efficient intracellular drug delivery and controlled drug release in cancer therapy. Subsequently, the fluorescence images of the FCSP@DOX were taken after being incubated with 4T1 cells for 6 h to explore NIR-promoted DOX uptake. As shown in Supporting Information Fig. S11, the red fluorescence intensity in FCSP@DOX group slightly improved after NIR irradiation was applied, implying that the temperature increase caused by NIR could improve the permeability of the cellular membrane for easier DOX uptake through affecting the fluidity of the membrane, molecular movement and the stability of the membrane[54,55]. The successful delivery of DOX could not only achieve cancer chemotherapy, but also generate H_2O_2 through the catalysis of the NADPH,

amplifying tumor-specific H_2O_2 level[49]. The amplified H_2O_2 was verified following a reported method by using DCFH-DA. The increasing green fluorescence in 4T1 cells indicated the generation of H_2O_2 with the accumulation of DOX (Supporting Information Fig. S12).

Afterward, the anti-tumor effect of the FCSP@DOX MOFs was identified by incubating them with 4T1 cells under different conditions. The ROS generation was firstly determined. As shown in Fig. 4A, compared with the control group and NIR only group, increasing green fluorescence in the FCSP MOFs group could be observed. After the addition of 10 mmol/L GSH, the ROS level in MOFs group was remarkably enhanced. This phenomenon can be attributed to that GSH can lead to degradation of MOFs, releasing Fe and Cu dual ions to activate Fenton or Fenton-like reaction. In addition, the green fluorescence became much brighter after NIR irradiation, proving that photothermal can promote Fenton reaction to generate more ·OH, which was beneficial to strengthen the therapeutic effect of ferroptosis based chemodynamic therapy. The flow cytometric analysis (Fig. 4B and C), which were consistent to the results of fluorescence images, further verified that FCSP MOFs possessed the ability of ROS generation through Fenton reaction and the level of ROS generation could be further enhanced by GSH-induced degradation of MOFs and NIR irradiation.
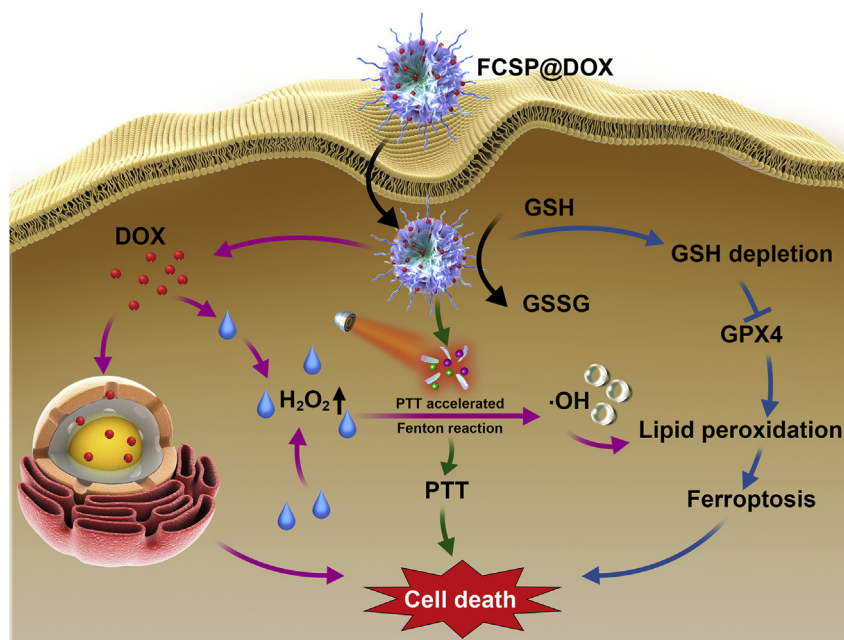
Scheme 2 Schematic illustration of the TME self-activated FCSP@DOX MOFs for ferroptosis based cancer chemodynamic/photothermal/chemo therapy. Ferroptosis based chemodynamic therapy would be activated by the redox tumor environment due to GSH depletion induced GPX4 inhibition and Fe/Cu ions involved Fenton reaction. More ROS could be generated by the acceleration of Fenton reaction due to the intrinsic photothermal capability of FCSP MOFs. Moreover, the released DOX could not only induce chemotherapy, but also indirectly produce H_2O_2 to further enhance the ferroptosis based cancer chemodynamic therapy.

The anticancer therapeutic efficacy of the FCSP@DOX MOFs under different conditions was then assessed by MTT assay (Fig. 4D). Comparing with slightly toxic 62.5 μg/mL FCSP group, FCSP in the exist of 10 mmol/L GSH possessed significant efficiency to inhibit cancer cells, illustrating that the disassembly of FCSP MOFs triggered by GSH increased Fe and Cu ions exposure to cancer cells for ·OH generation. In addition, the anti-tumor effect became more evident with NIR irradiation, suggesting that NIR-induced hyperthermia can not only produce photothermal therapy, but also promote Fenton reaction to generate more ·OH for enhancing Fenton reaction and inducing ferroptosis (the temperature was kept at around 46 °C monitored by an infrared thermal imaging system). On the other hand, FCSP@DOX could suppress cells growth with the cell viability about 70%, indicating that DOX had been successfully wrapped inside the MOFs and there was only limited leakage without other stimulation. The GSH-triggered cleavage could not only release metal ions for ferroptosis based chemodynamic therapy, but also fulfill chemotherapy due to the release of DOX, and therefore better therapeutic effect could be obtained. Further treatment with NIR irradiation could perform the best anti-tumor effect due to the synchronous ferroptosis-based chemodynamic/photothermal/chemo therapy (FCSP@DOX +10 mmol/L GSH + NIR group). The schematic illustration of the TME self-activated FCSP@DOX MOFs for ferroptosis based cancer chemodynamic/photothermal/chemo therapy was concluded and shown in Scheme 2.

3.4. In vivo anti-tumor activity by redox TME self-activated ferroptosis based chemodynamic/photothermal/chemo therapy

Encouraged by the excellent outcomes *in vitro*, *in vivo* TME self-activated ferroptosis based chemodynamic/photothermal/chemo therapy of the MOFs was investigated. 4T1 tumor-bearing mice

were intravenously injected by different FCSP@DOX formulation and control formulations, with or without 808 nm laser irradiation. Tumor volume and relative body weights were calculated to assess the anti-tumor effect every two days (Fig. 5A and B). The tumors in FCSP group possessed mild tumor growth inhibition compared with PBS group, indicating the FCSP MOFs had the ability to induce ferroptosis for cancer therapy by GSH depletion and ROS generation. The synergistic ferroptosis based chemodynamic/chemo therapy treatment group (FCSP@DOX group) had the increased tumor suppression than mono-therapy groups (FCSP and free DOX groups), which demonstrated that synergistic ferroptosis based chemodynamic/chemotherapy can reinforce therapeutic efficiency. When the NIR (808 nm) irradiation was applied, the temperature of the tumor area in either FCSP or FCSP@DOX group could increase and kept around 46 °C (Supporting Information Fig. S13), which is much higher than PBS group and enough to accelerate Fenton reaction to generate more ·OH for ferroptosis based chemodynamic therapy. The involving of mild-photothermal had more significant cancer inhibition than that without NIR irradiation, due to the enhanced ferroptosis-based chemodynamic therapy. The tumors of FCSP@DOX + NIR group were evidently inhibited both in volume (Fig. 5A and Supporting Information Fig. S14) and in weight (Fig. 5C). FCSP@DOX + NIR group achieved the best growth inhibition rate of tumor. Based on these results, FCSP@DOX MOFs have shown an excellent anti-tumor ability *in vivo via* TME-activated ferroptosis based chemodynamic/photothermal/chemo therapy. There were no significant differences in weight loss of the mice in each group (seen in Fig. 5B), demonstrating that the FCSP@DOX MOFs have no obvious system toxicity. After treatment, tumor tissues of each group were removed and stained with hematoxylin and eosin (H&E) and TUNEL to observe tumor morphology and apoptosis (Fig. 5D and Supporting Information Fig. S15). There
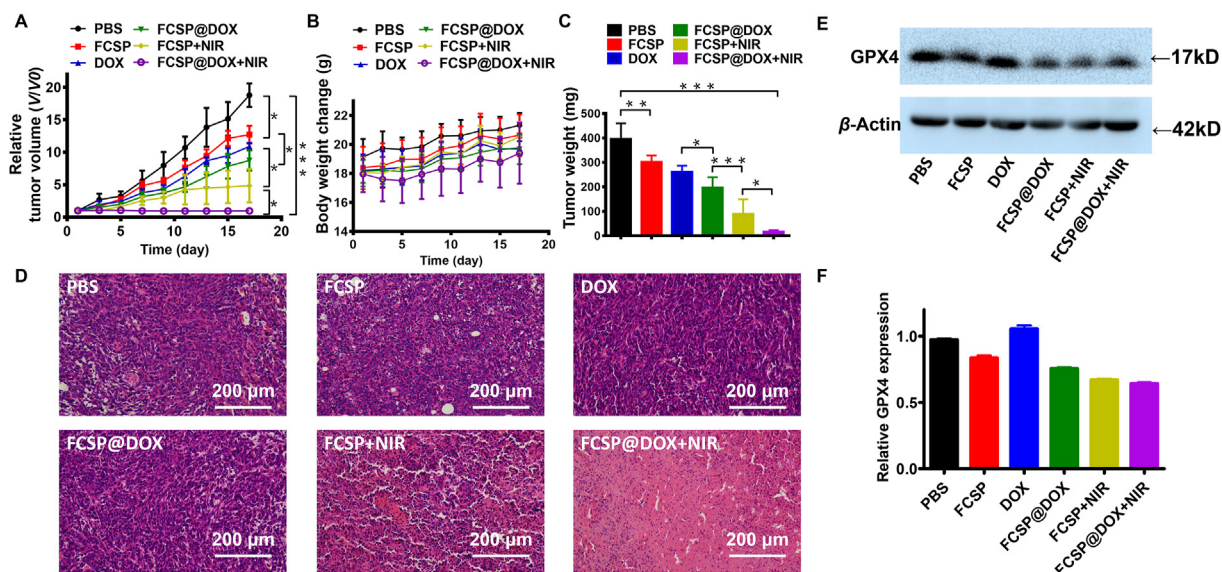
Figure 5 (A) The relative tumor growth curves (date are presented as mean ± SD (*n* = 5), *P < 0.05, **P < 0.01, ***P < 0.001) and (B) mice body weights change during the different treatments during the 18 days study period. (C) Tumor weight from sacrificed animals at the end of the experiment. Date are presented as mean ± SD (*n* = 5), *P < 0.05, **P < 0.01, ***P < 0.001. (D) H&E stained images of tumors tissues after different treatments (scale bar = 200 μm). (E) Western blot results of GPX4 expression level in 4T1 tumor tissue after different treatments, and (F) their relative quantification (*n* = 3).

was no apparent cell apoptosis in the PBS group and FCSP MOFs groups, while a slight cell apoptosis in the DOX group (Fig. S15) indicating that FCSP MOFs did not induce apoptosis. Cell apoptosis increased significantly in the combined groups (FCSP@DOX), indicating FCSP@DOX achieved higher drug availability and targeted delivery efficiency than free DOX. When NIR were employed, the H&E and TUNEL results showed the significantly improved therapeutic effect of tumor as it has been already well confirmed that photothermal therapy could not only induce apoptosis itself, but also lead to the deeper drug penetration by increased intratumoral blood flow through NIR-induced increasing temperature[56−59]. Furthermore, H&E staining of the major organs (heart, liver, spleen, lung, and kidney) in FCSP@DOX + NIR group indicated that there was not tissue necrosis, demonstrating that no significant adverse effects were noted for these treatments (Supporting Information Fig. S16). As for validating the mechanism of FCSP MOFs, the GPX4 level of tumor in every group was measured by Western blot. The results found that the GPX4 protein expression level decreased in all the groups containing FCSP MOF, demonstrating that FCSP MOF can down-regulate GPX4 expression by depleting its cofactor GSH to induce ferroptosis therapy while the DOX did not influence the expression of GPX4 (Fig. 5E and F).

3.5. Magnetic resonance (MR) and photoacoustic (PA) imaging properties

To our delight, FCSP@DOX also showed good magnetic resonance (MR) and photoacoustic (PA) Imaging capabilities. In details, FCSP@DOX samples showed a concentration-dependent signal changing with a linear correlation between concentration and the T2 relaxivity value under T2-weighted *in vitro* MR imaging (Supporting Information Fig. S17A). Then, FCSP@DOX

was intratumorally injected into 4T1 tumors in BALB/c mice. As shown in Figs. S17C and S17D, the MR imaging signals achieved a four-fold change after/before injection in the tumor area under T2-weighted *in vivo* MR imaging. PA imaging property of FCSP@DOX MOFS was also assessed *in vitro* and *in vivo*. According to Fig. S17B, FCSP@DOX showed a concentration-dependent rise of PA signal. There was a linear correlation between concentration and PA value. Moreover, the PA signals increased significantly in the tumor area after intratumoral injection of FCSP@DOX (Figs. S17E and S17F). These results indicated that the FCSP@DOX showed great potential to be MR and PA imaging agents.

4. Conclusions

In conclusion, for the first time, tumor microenvironment activated FCSP@DOX MOFs were constructed for ferroptosis-based cancer chemodynamic/photothermal/chemo therapy. The as-prepared FCSP@DOX MOFs could be accumulated in the tumor site through EPR effect, and disintegrated in overexpressed GSH tumor microenvironment because of GSH-induced breakage of disulfide bonds, therefore inducing ferroptosis by inhibition of GPX4 expression. Meanwhile, disintegration of FCSP@DOX MOFs leaded to gradually release of Fe, Cu ions and DOX. The release Fe & Cu dual ions could catalyze overexpressed H_2O_2 to toxic ·OH *via* Fenton or Fenton-like reaction. The inhibition of GPX4 and Fenton or Fenton-like reaction generated ROS together contributed to abundant lipid peroxidation, fulfilling ferroptosis based chemodynamic therapy. Furthermore, the intrinsic photothermal property could accelerate Fenton reaction for more ·OH generation. Moreover, the co-delivered DOX could not only achieve chemotherapy by blocking topoisomerase II, but also

generate H_2O_2 which may further amplify the therapeutic efficacy. This system could be specifically activated by the redox tumor microenvironment achieving excellent anti-tumor effect both *in vitro* and *in vivo* by taking the synergy of GSH-depletion assistant GPX4 inactivation and iron-dependent Fenton reaction induced ferroptosis, mild hyperthermia, and chemotherapy. Overall, the inherent TME-activated MOFs for non-apoptotic ferroptosis therapy would be significant for their potential clinical translation to assist or solve the problems of tumor apoptosis.

Acknowledgments

Author contributions

Bingxia Zhao and Yingjia Li as corresponding authors were responsible for experiment design, data collecting, data processing, paper writing, paper submitting and revision. Yu Liang, Li Zhang and Chao Peng as first authors were responsible for data collecting, data analysis, cell culture and animal experiment. Shiyu Zhang and Siwen Chen assisted the synthesis of MOFs. Xin Qian, Wanxian Luo assisted the *in vivo* therapeutic evaluations. Qing Dan and Yongyan Ren were in charge of imaging property of MOFs.

Conflicts of interest

The authors have no conflicts of interest to declare.

Appendix A.   Supporting information

Supporting data to this article can be found online at https://doi.org/10.1016/j.apsb.2021.01.016.

References

1. Dixon SJ, Lemberg KM, Lamprecht MR, Skouta R, Zaitsev EM, Gleason CE, et al. Ferroptosis: an iron-dependent form of non-apoptotic cell death. *Cell* 2012;**149**:1060−72.
2. Angeli JPF, Shah R, Pratt DA, Conrad M. Ferroptosis inhibition: mechanisms and opportunities. *Trends Pharmacol Sci* 2017;**38**:489−98.
3. Doll S, Proneth B, Tyurina YY, Panzilius E, Kobayashi S, Ingold I, et al. ACSL4 dictates ferroptosis sensitivity by shaping cellular lipid composition. *Nat Chem Biol* 2017;**13**:91−8.
4. Shimada K, Skouta R, Kaplan A, Yang WS, Hayano M, Dixon SJ, et al. Global survey of cell death mechanisms reveals metabolic regulation of ferroptosis. *Nat Chem Biol* 2016;**12**:497−503.
5. Shimada K, Hayano M, Pagano NC, Stockwell BR. Cell-line selectivity improves the predictive power of pharmacogenomic analyses and helps identify NADPH as biomarker for ferroptosis sensitivity. *Cell Chem Biol* 2016;**23**:225−35.
6. Cardoso BR, Hare DJ, Bush AI, Roberts BR. Glutathione peroxidase 4: a new player in neurodegeneration?. *Mol Psychiatr* 2017;**22**:328−35.
7. Gao M, Monian P, Quadri N, Ramasamy R, Jiang X. Glutaminolysis and transferrin regulate ferroptosis. *Mol Cell* 2015;**59**:298−308.
8. Hou W, Xie Y, Song X, Sun X, Lotze MT, Zeh HJ, et al. Autophagy promotes ferroptosis by degradation of ferritin. *Autophagy* 2016;**12**:1425−8.
9. Yang WS, SriRamaratnam R, Welsch ME, Shimada K, Skouta R, Viswanathan VS, et al. Regulation of ferroptotic cancer cell death by GPX4. *Cell* 2014;**156**:317−31.
10. Stockwell BR, Friedmann Angeli JP, Bayir H, Bush AI, Conrad M, Dixon SJ, et al. Ferroptosis: a regulated cell death nexus linking metabolism, redox biology, and disease. *Cell* 2017;**171**:273−85.
11. Sengupta A, Lichti UF, Carlson BA, Cat7aisson C, Ryscavage AO, Mikulec C, et al. Targeted disruption of glutathione peroxidase 4 in mouse skin epithelial cells impairs postnatal hair follicle morphogenesis that is partially rescued through inhibition of COX-2. *J Invest Dermatol* 2013;**133**:1731−41.
12. Ueta T, Inoue T, Furukawa T, Tamaki Y, Nakagawa Y, Imai H, et al. Glutathione peroxidase 4 is required for maturation of photoreceptor cells. *J Biol Chem* 2012;**287**:7675−82.
13. Jiang L, Kon N, Li T, Wang SJ, Su T, Hibshoosh H, et al. Ferroptosis as a p53-mediated activity during tumour suppression. *Nature* 2015;**520**:57−62.
14. Louandre C, Marcq I, Bouhlal H, Lachaier E, Godin C, Saidak Z, et al. The retinoblastoma (Rb) protein regulates ferroptosis induced by sorafenib in human hepatocellular carcinoma cells. *Cancer Lett* 2015;**356**:971−7.
15. Sun X, Niu X, Chen R, He W, Chen D, Kang R, et al. Metallothionein-1G facilitates sorafenib resistance through inhibition of ferroptosis. *Hepatology* 2016;**64**:488−500.
16. Sehm T, Fan Z, Ghoochani A, Rauh M, Engelhorn T, Minakaki G, et al. Sulfasalazine impacts on ferroptotic cell death and alletes the tumor microenvironment and glioma-induced brain edema. *Oncotarget* 2016;**7**:36021−33.
17. Ooko E, Saeed MEM, Kadioglu O, Sarvi S, Colak M, Elmasaoudi K, et al. Artemisinin derivatives induce iron-dependent cell death (ferroptosis) in tumor cells. *Phytomedicine* 2015;**22**:1045−54.
18. Eling N, Reuter L, Hazin J, Hamacher-Brady A, Brady NR. Identification of artesunate as a specific activator of ferroptosis in pancreatic cancer cells. *Oncoscience* 2015;**2**:517−32.
19. Scott J, Dixon BRS. The hallmarks of ferroptosis. *Annu Rev Cell Biol* 2019;**3**:35−54.
20. Wang S, Liao H, Li F, Ling D. A mini-review and perspective on ferroptosis-inducing strategies in cancer therapy. *Chin Chem Lett* 2019;**30**:847−52.
21. Shen Z, Song J, Yung BC, Zhou Z, Wu A, Chen X. Emerging strategies of cancer therapy based on ferroptosis. *Adv Mater* 2018;**30**:1704007.
22. Meng X, Deng J, Liu F, Guo T, Liu M, Dai P, et al. Triggered all-active metal organic framework: ferroptosis machinery contributes to the apoptotic photodynamic antitumor therapy. *Nano Lett* 2019;**19**:7866−76.
23. Shan X, Li S, Sun B, Chen Q, Sun J, He Z, et al. Ferroptosis-driven nanotherapeutics for cancer treatment. *J Control Release* 2020;**319**:322−32.
24. Szatrowski TP, Nathan CF. Production of large amounts of hydrogen peroxide by human tumor cells. *Cancer Res* 1991;**51**:794−8.
25. Dan Q, Hu D, Ge Y, Zhang S, Li S, Gao D, et al. Ultrasmall theranostic nanozymes to modulate tumor hypoxia for augmenting photodynamic therapy and radiotherapy. *Biomater Sci* 2020;**8**:973−87.
26. Huo M, Wang L, Chen Y, Shi J. Tumor-selective catalytic nanomedicine by nanocatalyst delivery. *Nat Commun* 2017;**8**:357.
27. An Q, Sun C, Li D, Xu K, Guo J, Wang C. Peroxidase-like activity of Fe_3O_4@carbon nanoparticles enhances ascorbic acid-induced oxidative stress and selective damage to PC-3 prostate cancer cells. *ACS Appl Mater Interfaces* 2013;**5**:13248−57.

28. Zanganeh S, Hutter G, Spitler R, Lenkov O, Mahmoudi M, Shaw A, et al. Iron oxide nanoparticles inhibit tumour growth by inducing pro-inflammatory macrophage polarization in tumour tissues. *Nat Nanotechnol* 2016;**11**:986−94.

29. Zhang C, Bu W, Ni D, Zhang S, Li Q, Yao Z, et al. Synthesis of iron nanometallic glasses and their application in cancer therapy by a localized Fenton Reaction. *Angew Chem Int Ed Engl* 2016;**55**: 2101−6.

30. Bi H, Dai Y, Yang P, Xu J, Yang D, Gai S, et al. Glutathione mediated size-tunable UCNPs-Pt(IV)-ZnFe$_2$O$_4$ nanocomposite for multiple bioimaging guided synergetic therapy. *Small* 2018;**14**:e1703809.

31. Tang Z, Liu Y, He M, Bu W. Chemodynamic therapy: tumour microenvironment-mediated Fenton and fenton-like reactions. *Angew Chem Int Ed Engl* 2019;**58**:946−56.

32. Cai W, Wang J, Chu C, Chen W, Wu C, Liu G. Metal-organic framework-based stimuli-responsive systems for drug delivery. *Adv Sci (Weinh)* 2019;**6**:1801526.

33. Zheng DW, Lei Q, Zhu JY, Fan JX, Li CX, Li C, et al. Switching apoptosis to ferroptosis: metal-organic network for high-efficiency anticancer therapy. *Nano Lett* 2017;**17**:284−91.

34. Ranji-Burachaloo H, Karimi F, Xie K, Fu Q, Gurr PA, Dunstan DE, et al. MOF-mediated destruction of cancer using the cell's own hydrogen peroxide. *ACS Appl Mater Interfaces* 2017;**9**:33599−608.

35. Hu P, Wu T, Fan W, Chen L, Liu Y, Ni D, et al. Near infrared-assisted Fenton reaction for tumor-specific and mitochondrial DNA-targeted photochemotherapy. *Biomaterials* 2017;**141**:86−95.

36. Tang Z, Zhang H, Liu Y, Ni D, Zhang H, Zhang J, et al. Antiferromagnetic pyrite as the tumor microenvironment-mediated nanoplatform for self-enhanced tumor imaging and therapy. *Adv Mater* 2017; **29**:1701683.

37. Hu R, Fang Y, Huo M, Yao H, Wang C, Chen Y, et al. Ultrasmall Cu$_{2-x}$S nanodots as photothermal-enhanced Fenton nanocatalysts for synergistic tumor therapy at NIR-II biowindow. *Biomaterials* 2019;**206**: 101−14.

38. Nie X, Xia L, Wang HL, Chen G, Wu B, Zeng TY, et al. Photothermal therapy nanomaterials boosting transformation of Fe(III) into Fe(II) in tumor cells for highly improving chemodynamic therapy. *ACS Appl Mater Interfaces* 2019;**11**:31735−42.

39. Sun M, Shahzeydi A. Facile and green synthesis of copper nanoparticles loaded on the amorphous carbon nitride for the oxidation of cyclohexane. *Chem Eng J* 2019;**370**:1310−21.

40. Cramer SL, Saha A, Liu J, Tadi S, Tiziani S, Yan W, et al. Systemic depletion of L-cyst(e)ine with cyst(e)inase increases reactive oxygen species and suppresses tumor growth. *Nat Med* 2017;**23**:120−7.

41. Wang S, Li F, Qiao R, Hu X, Liao H, Chen L, et al. Arginine-rich manganese silicate nanobubbles as a ferroptosis-inducing agent for tumor-targeted theranostics. *ACS Nano* 2018;**12**:12380−92.

42. Fan H, Yan G, Zhao Z, Hu X, Zhang W, Liu H, et al. A smart photosensitizer-manganese dioxide nanosystem for enhanced photodynamic therapy by reducing glutathione levels in cancer cells. *Angew Chem Int Ed Engl* 2016;**55**:5477−82.

43. Lin LS, Song J, Song L, Ke K, Liu Y, Zhou Z, et al. Simultaneous Fenton-like ion delivery and glutathione depletion by MnO$_2$-based nanoagent to enhance chemodynamic therapy. *Angew Chem Int Ed Engl* 2018;**57**:4902−6.

44. Diehn M, Cho RW, Lobo NA, Kalisky T, Dorie MJ, Kulp AN, et al. Association of reactive oxygen species levels and radioresistance in cancer stem cells. *Nature* 2009;**458**:780−3.

45. Ross D. Glutathione, free radicals and chemotherapeutic agents. Mechanisms of free-radical induced toxicity and glutathione-dependent protection. *Pharmacol Therapeut* 1988;**37**:231−49.

46. Arrick BA, Nathan CF. Glutathione metabolism as a determinant of therapeutic efficacy: a review. *Cancer Res* 1984;**44**:4224−32.

47. Liu T, Liu W, Zhang M, Yu W, Gao F, Li C, et al. Ferrous-supply-regeneration nanoengineering for cancer-cell-specific ferroptosis in combination with imaging-guided photodynamic therapy. *ACS Nano* 2018;**12**:12181−92.

48. Sang M, Luo R, Bai Y, Dou J, Zhang Z, Liu F, et al. Mitochondrial membrane anchored photosensitive nano-device for lipid hydroperoxides burst and inducing ferroptosis to surmount therapy-resistant cancer. *Theranostics* 2019;**9**:6209−23.

49. Wang S, Yang L, Cho HY, Dean CST, Zhang H, Zhang Q, et al. Programmed degradation of a hierarchical nanoparticle with redox and light responsivity for self-activated photo-chemical enhanced chemodynamic therapy. *Biomaterials* 2019;**224**:119498.

50. Peng C, Liang Y, Chen Y, Qian X, Luo W, Chen S, et al. Hollow mesoporous tantalum oxide based nanospheres for triple sensitization of radiotherapy. *ACS Appl Mater Interfaces* 2020;**12**:5520−30.

51. Yan N, Lin L, Xu C, Tian H, Chen X. A GSH-gated DNA nanodevice for tumor-specific signal amplification of microRNA and MR imaging-guided theranostics. *Small* 2019;**15**:1903016.

52. Wang F, Huang Q, Wang Y, Shi L, Shen Y, Guo S. NIR-light and GSH activated cytosolic p65-shRNA delivery for precise treatment of metastatic cancer. *J Control Release* 2018;**288**:126−35.

53. Li S, Saw PE, Lin C, Nie Y, Tao W, Farokhzad OC, et al. Redox-responsive polyprodrug nanoparticles for targeted siRNA delivery and synergistic liver cancer therapy. *Biomaterials* 2020;**234**:119760.

54. Jeong WC, Kim SH, Yang SM. Photothermal control of membrane permeability of microcapsules for on-demand release. *ACS Appl Mater Interfaces* 2014;**6**:826−32.

55. Torchi A, Simonelli F, Ferrando R, Rossi G. Local enhancement of lipid membrane permeability induced by irradiated gold nanoparticles. *ACS Nano* 2017;**11**:12553−61.

56. Wang J, Wang X, Lu S, Hu J, Zhang W, Xu L, et al. Integration of cascade delivery and tumor hypoxia modulating capacities in core-releasable satellite nanovehicles to enhance tumor chemotherapy. *Biomaterials* 2019;**223**:119465.

57. Wen Y, Chen X, Zhu X, Gong Y, Yuan G, Qin X, et al. Photothermal-chemotherapy integrated nanoparticles with tumor microenvironment response enhanced the induction of immunogenic cell death for colorectal cancer efficient treatment. *ACS Appl Mater Interfaces* 2019; **11**:43393−408.

58. Yang Z, Cheng R, Zhao C, Sun N, Luo H, Chen Y, et al. Thermo- and pH-dual responsive polymeric micelles with upper critical solution temperature behavior for photoacoustic imaging-guided synergistic chemo-photothermal therapy against subcutaneous and metastatic breast tumors. *Theranostics* 2018;**8**:4097−115.

59. Zhang L, Zhang S, Chen H, Liang Y, Zhao B, Luo W, et al. An acoustic/thermo-responsive hybrid system for advanced doxorubicin delivery in tumor treatment. *Biomater Sci* 2020;**8**:2202−11.